Park Ho Seok (Orcid ID: 0000-0002-4424-4037)
Lee Lawrence Yoon Suk (Orcid ID: 0000-0002-6119-4780)

DOI: 10.1002/ ((please add manuscript number))
Article type: Full Paper

Sodium-coordinated polymeric phthalocyanines as stable high-capacity organic anodes for sodium-ion batteries

Jeongyeon Lee,† Yoonbin Kim,† Soyong Park, Kang Ho Shin, Gun Jang, Min Jun Hwang, Daekyu Kim, Kyung-Ah Min, Ho Seok Park, Byungchan Han,* Dennis K. P. Ng,* and Lawrence Yoon Suk Lee*

Dr. Jeongyeon Lee; Daekyu Kim; Prof. Lawrence Yoon Suk Lee
Department of Applied Biology and Chemical Technology and Research Institute for Smart Energy
The Hong Kong Polytechnic University, Hung Hom, Kowloon, Hong Kong SAR

Dr. Yoonbin Kim; Prof. Dennis K. P. Ng
Department of Chemistry, The Chinese University of Hong Kong, Shatin, New Territories, Hong Kong SAR, China

Dr. Yoonbin Kim
Convergence Research Center for Energy and Environmental Sciences, Sungkyunkwan University, Suwon, Republic of Korea

Soyong Park; Dr. Kyung-Ah Min; Prof. Byungchan Han
Department of Chemical and Biomolecular Engineering, Yonsei University, Seoul, Republic of Korea

Kang Ho Shin; Gun Jang; Min Jun Hwang; Prof. Ho Seok Park
School of Chemical Engineering, Sungkyunkwan University, Suwon, Republic of Korea

† These authors contributed equally

E-mails: bchan@yonsei.ac.kr (B. Han); dkpn@cuhk.edu.hk (D. K. P. Ng); lawrence.ys.lee@polyu.edu.hk (L. Y. S. Lee)

Keywords: phthalocyanine; coordination chemistry; polymerization; organic anode; sodium ion battery

Abstract

Sodium-ion batteries (SIBs) have attracted considerable interest as an alternative to lithium-ion batteries owing to their similar electrochemical performance and superior long-term cycle stability. Organic materials are regarded as promising anode materials for constructing SIBs with high capacity and good retention. However, utilization of organic materials is rather limited by their low energy density and poor stability at high current densities. To overcome these limitations, we utilized a novel polymeric disodium phthalocyanines (*p*NaPc) as SIB anodes to provide stable coordination sites for Na ions as well as to enhance the stability at high current density. By varying the linker type during a one-pot cyclization and polymerization process, two *p*NaPc anodes with O- (O-*p*NaPc) and S-linkers (S-*p*NaPc) were prepared, and their structural and electrochemical properties were investigated. The O-*p*NaPc binds Na ions with a lower binding energy compared with S-*p*NaPc, which leads to more facile Na-ion coordination/dissociation when engaged as SIB anode. The use of O-*p*NaPc significantly improves the redox kinetics and cycle stability and allows the fabrication of a full cell against $Na_3V_2(PO_4)_2F_3$/C cathode, which demonstrates its practical application with high energy density (288 Wh kg^{-1}) and high power density (149 W kg^{-1}).

1. Introduction

Concerns regarding worsening environmental problems such as global warming and air pollution have urged the development of green and sustainable energy systems.[1] Rechargeable batteries play a crucial role in such energy systems for storing renewable yet intermittent energies. Currently, lithium-ion batteries (LIBs) have an indispensable position in the portable electronics market owing to their high energy density.[2] However, with the rapid expansion of the electric vehicle industry, the demand for LIBs has surged, and their production costs have increased due to the excessive consumption of the limited and geographically unevenly distributed lithium reserves. It is thus imperative to develop alternative rechargeable batteries. Sodium-ion batteries (SIBs), which are based on the same working principles as LIBs, are considered a promising alternative to LIBs because of their lower cost and the abundance, as well as worldwide distribution of sodium reserves.[3] However, the larger ionic radius of Na results in poor diffusivity and severe volume expansion during battery cycling.[4] Moreover, the smooth transition from LIBs to SIBs is hampered by the incompatible internal compartments. For example, graphite, a conventional anode material for LIBs, is not suitable for SIBs due to its unfavorable intercalation of Na ions.[5] Hence, suitable electrodes, especially anodes, must be developed to improve the electrochemical performance and stability of SIBs.

One strategy to develop anodes for SIBs is by utilizing organic compounds that can provide stable coordination sites for Na ions, instead of conventional inorganic materials. Organic materials have several advantages over inorganic materials, such as their ease of disposal/recycling and environmental friendliness. More importantly, they can be readily modified with diverse functional groups that lead to rapid redox reactions of Na ions during cycling.[6] The weak binding interaction of organic electrodes with metal ions enables reversible electrochemical reactions with fast kinetics.[7] In particular, aromatic organics containing carboxylate groups have been often utilized as SIB anodes because the bonding

between carboxylates and Na ions can stabilize the Na intercalation. For a representative example, sodium terephthalate was used as an organic SIB anode to achieve a high specific capacity of over 290 mA h g^{-1} with good cycling stability.[8] In recent years, various organic anodes have been developed to enhance the electrochemical properties and stability of SIBs.[9] Recently, Glocklhofer *et al.*[10] engaged a conjugated macrocycle, [2.2.2.2]paracyclophane-1,9,17,25-tetraene, as the anode for SIBs, which stabilized the neutral state by local aromaticity and the doubly reduced state by global aromaticity, and demonstrated good capacity and stability under fast-charge/discharge conditions.

Phthalocyanines (Pc) are another promising class of aromatic organic materials that have been widely used in electrochemical applications owing to their unique and tuneable electronic and electrochemical properties.[11] Their N_4-macrocyclic core allows binding with a range of metal ions, including Na, to form stable metallophthalocyanine (MPc) complexes. Moreover, the electrical conductivity and thermal stability of these materials can be tuned by modifying their peripheral substituents[12] or by polymerization.[13] The latter can reduce the Pc solubility in various solvents and induce a synergetic effect with the substrate on which they are polymerized. Several methods have been developed to prepare polymerized metallophthalocyanines (*p*MPcs) from 1,2,4,5-tetracyanobenzene or phthalonitrile dimers (with linkers conjugated to the phthalonitrile precursors).[13a, 13b] The properties imparted by the metal center and peripheral substituents make *p*MPcs suitable as the catalysts for CO_2 reduction,[13a] oxygen evolution, and oxygen reduction reactions,[13c] as well as nitrite sensors.[13b] In our previous work, we reported a novel strategy to prepare polymeric cobalt phthalocynines (*p*CoPcs) with S- or SO_2-linker and showed that these *p*CoPcs functioned as efficient water-splitting electrocatalysts.[14] So far, the metal centers of *p*MPcs have been mostly utilized as catalytic sites. However, the Pc core can act as stable coordination sites for small metal ions such as Li and Na ions. Until now, the use of sodiated Pcs (NaPcs) in the energy storage field has not been reported.

In this work, we utilized Na ion-coordinated polymeric Pcs (*p*NaPcs) as anode material to build high-performing SIBs. We first synthesized the *p*NaPcs linked with either ether or thioether moieties and studied their electrochemical properties as the organic anode in SIBs. A facile one-step polymerization and cyclization approach was used to complex two Na ions at each Pc core and to connect the Pc units with ether or thioether linkers. The use of O- and S-linked polymeric Pcs can fine-tune the electrochemical properties of the resulting *p*NaPcs. The anodes fabricated with O- and S-*p*NaPcs were able to reversibly coordinate and release Na ions, and this process was dependent on the peripheral substituents. In electrochemical tests, both O- and S-*p*NaPc electrodes showed excellent cycle stability and reversible capacity. X-ray photoelectron spectroscopy (XPS) and density functional theory (DFT) calculations revealed that the coordination of Na ions with the isoindolic N atoms of the Pc core was stronger in S-*p*NaPc than in O-*p*NaPc, and this difference was reflected in their electrochemical performance in SIBs. To further understand the coordination/dissociation mechanism of the *p*NaPc SIB anodes, we conducted *ex situ* Raman spectroscopic studies to map the O-*p*NaPc anode after charging and discharging. A practical application of the *p*NaPc SIB anodes was demonstrated by performing a full-cell test against the well-known $Na_3V_2(PO_4)_2F_3$ (NVPF)/C cathode. The overall results demonstrate a novel and effective approach for manipulating the molecular structure of organic anode materials to realize stable and high-performance SIBs.

2. Results and discussion

Despite the environmental and economic benefits of using organic materials, the stability and capacity of SIBs made of organic anodes are limited by the lack of stable binding sites for Na ions. This can be attributed to the intrinsic instability of organic compounds under fast charging/discharging and long-term cycling conditions.[9e] To circumvent these limitations, we utilized *p*NaPcs in which the Pc cores were used as stable coordination sites for Na ions to

enhance the cycling stability. **Figure 1a** is a schematic illustration of the *p*NaPc synthetic procedure. First, two bisphthalonitriles, namely R–Pn (R = S or O) dimers, were prepared and characterized by ^{1}H and $^{13}C\{^{1}H\}$ NMR spectroscopy (**Figures S1** and **S2**, Supporting Information). The ^{1}H NMR spectra of both O–Pn and S–Pn dimers show the corresponding proton peaks at the aromatic region and aliphatic region. Also, $^{13}C\{^{1}H\}$ NMR spectra identify the corresponding carbon peaks, supporting successful preparation and purification of Pn dimers. 1-Pentanol was used as the solvent to dissolve Na metal, and the resulting $NaOC_5H_{11}$ suspension was used to prepare S- and O-*p*NaPcs from their respective Pn dimers. With these pre-linked precursors, *p*NaPcs could be synthesized *via* a facile one-step cyclization and polymerization procedure. **Figures 1b** and **1c** show the proposed structure and morphology of S- and O-*p*NaPcs, respectively. The morphology and composition of the as-prepared S- and O-*p*NaPcs were characterized using TEM and the corresponding energy-dispersive X-ray (EDX) elemental mapping. The uniform distribution of Na and other relevant elements (C, N, and O or S) indicates that Na ions are coordinated to the polymeric Pcs. The SEM images of *p*NaPcs (**Figure S3**) show small amorphous particles (average size = *ca.* 1 – 2 μm) aggregated into bulkier particles, which is caused by the vigorous stirring adopted to minimize over-polymerization to a bulk morphology. The X-ray diffraction (XRD) patterns of S-*p*NaPc and O-*p*NaPc shown in **Figure S4** further support their amorphous structures. The monomeric compounds (H_2Pc and NaPc) display XRD patterns arising from the self-assembled molecules owing to the strong π–π interaction, whereas the *p*NaPcs show featureless patterns.

The formation of *p*NaPc was further confirmed using various spectroscopic analyses. The UV–vis spectra in DMF show the signature Q-band absorptions of Pcs in the 650–750 nm region (**Figure 2a**). Compared with the commercial monomeric disodium phthalocyanine (NaPc), both *p*NaPcs show red-shifted Q-bands due to their electron-donating substituents (O or S). The stronger electron-donating nature of the thioether groups induces a greater shift in the Q-bands of S-*p*NaPc (*ca.* 683 and 712 nm) compared with O-*p*NaPc (*ca.* 670 and 703 nm).

Both *p*NaPcs and NaPc display the unique Q-band splitting characteristic of metal-free Pcs (H_2Pcs) owing to their lower symmetry, whereas single metal-coordinated Pcs generate a single Q-band.[15] The Q-bands of Pc monomers show a higher intensity than the B-bands, as evidenced by the sharp and strong Q-bands of NaPc. The suppressed Q-bands of *p*NaPcs, compared with the B-band, reflect the degree of polymerization[16] and confirm the successful polymerization of both Pcs. The FT-IR spectra of *p*NaPcs (**Figure 2b**) show the characteristic vibration peaks corresponding to the C=N (*ca.* 1,663 cm^{-1}), C=C (*ca.* 1,601 cm^{-1}), C–C (*ca.* 1,463 and 1,388 cm^{-1}), and C–H (*ca.* 1,095, 1,012, and 750 cm^{-1}) stretches of Pc macrocycles, as well as the C–O (*ca.* 1,220 and 1,050 cm^{-1}) or C–S (*ca.* 663 cm^{-1}) stretches of the linkers.[17] The cyclization and metal complexation of Pcs are confirmed by Raman spectroscopy (**Figure 2c**). The A_{1g}, B_{2g}, and B_{1g} bands located at *ca.* 684, 1,403, and 1,528 cm^{-1}, respectively, are ascribable to the isoindole C–N–C stretch, and the B_{1g} and two A_{1g} bands at *ca.* 801, 1,110, and 1,329 cm^{-1}, respectively, are assignable to the isoindole N–M stretch.[18] These peaks indicate the interaction between the Pc core and Na ions. Moreover, the broad bands at *ca.* 1,600 cm^{-1} are attributable to the C–C and C–O/S vibrations of the conjugated linkers.

The linkers in *p*NaPcs offer a convenient way of tuning their physicochemical properties by the substituent effect. XPS was used to probe the surface electronic states and elemental compositions of these compounds. The survey XPS spectra displayed in **Figure S5** indicate the presence of all expected elements, and the strong O signals are due to the inevitable oxidation caused by air exposure.[18] Although a strong signal for adsorbed O is observed in both *p*NaPcs, the intensity of the O1 peak, which corresponds to C–O/C=O, is higher in the O-*p*NaPcs, an observation that supports the presence of the O-linker. The surface-adsorbed O2 peak also shifts to higher binding energy (+0.3 eV) owing to the different surface chemical energies of the two *p*NaPcs, whereas the O3 peak of the O in H_2O remains at the

same binding energy (**Figure S6a**).[19] Notably, the absence of a peak corresponding to the Na–O bonding (529 eV) further supports that Na ions are not bound to the oxygen linker.[20]

Similarly, the presence of the S-linker in S-*p*NaPc is reflected in the deconvoluted peaks at 163.2 and 164.4 eV, which correspond to the S $2p_{3/2}$ and S $2p_{1/2}$ of the C–S–C bond, respectively, without any peaks related to Na–S bonding (**Figure S6b**).[21] The high-resolution C 1s spectrum of O-*p*NaPc in **Figure 2d** can be deconvoluted into four peaks: C1 (C–C, 284.3 eV), C2 (C–N, 284.9 eV), C3 (C=N, 285.9 eV), and C4 (C–O, 288.9 eV). S-*p*NaPc also exhibits similar C1–C3 peaks and the C5 peak corresponding to the C–S bond appears at 288.4 eV.[22] Interestingly, the C2 peak of S-*p*NaPc is located at a higher binding energy (+0.1 eV) than that of O-*p*NaPc, and similar peak shifts are observed in the high-resolution N 1s spectra in **Figure 2e**. The N1 (bridging N, 398.1 eV) and N2 (pyrrolic N, 399.6 eV) peaks of S-*p*NaPc are shifted by +0.1 and +0.2 eV, respectively, compared with those of O-*p*NaPc.[23] These shifts are attributed to the thioether substituents having a higher electron density and a stronger electron-donating nature than the ether substituents.[24] More importantly, the N2 peak is known to correspond to the N species associated with Na metal,[24b] which indicates successful coordination of Na ions at the core of Pc unit. Thus, the Pc core with thioether substituents coordinates more strongly with Na ions as it polarizes the pyrrolic N more than the Pc core with ether substituents as manifested by the binding energy shifts. This is further supported by the blue-shifted (0.2 eV) Na 1s spectrum of S-*p*NaPc (**Figure 2f**), which indicates the more negative character of the Na ions in S-*p*NaPc than those in O-*p*NaPc. The chemical shift in the Na 1s spectra and the absence of Na–O/S peak verify that the Na ions are coordinated with the Pc core rather than with the linker, and the binding energy of Na ions is influenced by the properties of the linkage substituents.

To elucidate the underlying mechanism of the Na ion interaction in *p*NaPcs, first-principles DFT calculations were conducted using O-*p*NaPcs and S-*p*NaPcs modelled in periodic boundary conditions, as shown in **Figure 3a**. We characterized their spectral features

by calculating the highest-occupied molecular orbital (HOMO)–lowest-unoccupied molecular orbital (LUMO) gaps. **Figure S7** shows that the HOMO–LUMO gaps of S- and O-*p*NaPcs are 1.14 and 1.10 eV, respectively. Considering that the Q-band red-shift is caused by the destabilization of HOMO relative to LUMO, the red-shift of S-*p*NaPc should be more conspicuous than that of O-*p*NaPc. The destabilization of O-*p*NaPc is more apparent than that of S-*p*NaPc because the thioether linkage has a stronger electron-donating nature than the ether linkage. Based on these results, we identified the active binding sites for Na ions in the intercalation process. The metal center (Site 1), aromatic ring (Site 2), and void (Site 3) sites were explicitly calculated as indicated in **Figure 3a**. The binding energy (E_b) of the Na ion at each site was calculated using Equation (1):

$$E_b = E_{fin} - (E_{init} + E_{Na}) \qquad (1)$$

where E_{init}, E_{fin}, and E_{Na} represent the total energy of Pc with one Na ion at the metal center, Pc with an additional Na ion at each site and Na metal, respectively. The optimized structures with bound Na are shown in **Figures S8** and **S9**. As summarized in **Table S1** (Supporting information), the metal center (Site 1) has the strongest interaction for both O- and S-*p*NaPcs, forming bonds that have intensities comparable to ionic bonds with the isoindolic N. Since Na ions are forming bonds with Pc^{2-} that is a conjugate base of H_2Pc, the calculated binding energies comparable to the intensity of ionic bonds are reasonable.[25] The other two sites have weaker bindings, as indicated by the E_b and structures. Notably, S-*p*NaPc has a larger binding strength than O-*p*NaPc. This result is consistent with the spectroscopic observation that S-*p*NaPc coordinates strongly with the Na ions. Our DFT results suggest that the sodiation/desodiation processes can be facilitated in O-*p*NaPc due to the weaker Na ion binding with the isoindolic N at the metal center compared with the case of S-*p*NaPc.

We further analyzed the electronic structures of the metal center using the projected density of states (PDOS) approach. **Figures 3b** and **3c** show the PDOS for N, O (or S), and Na in O- and S-*p*NaPcs, respectively. The prominent Na peaks are marked by yellow arrows.

In S-*p*NaPc, the hybridization of the N and Na electronic states results in strong structural coordination. In contrast, there is a strong hybridization between the N and O in O-*p*NaPc, and the N and Na exhibit weak interactions. These results can be attributed to the electronic structure mechanism that generates a weaker E_b in O-*p*NaPc than in S-*p*NaPc. Both DFT calculation outcomes suggest that the substituents in linkage can tune the binding energy of Na ions with Pc core, which can lead to the performance difference when applied as the anode in SIBs.

To evaluate the coordination/dissociation of the Na ion in the *p*NaPc structure during the charging and discharging processes, we prepared pristine, discharged, and charged O-*p*NaPc anodes according to the galvanostatic profile shown in **Figure 4a** and used them for *ex situ* analysis. For qualitative analyses, these anodes were cycled twice at a current density of 50 mA g^{-1} in a potential window between 0.01 and 2.0 V. The first couple of cycles are crucial for enhancing the accuracy of the analysis because they are responsible for the formation of the solid electrolyte interphase (SEI) layers on the anode.[26] The charged anode was taken from the cell immediately after the charging process of the second cycle, whereas the discharged anode was taken from the cell after an additional discharging process. To prevent the oxidation of Na metal, which could interfere with the analysis, both cells were disassembled in an Ar-filled glovebox and thoroughly washed with ethanol to remove any residual electrolyte. The Na 1s XPS spectra of the charged and discharged O-*p*NaPc anodes (**Figure 4b**) show an additional peak at 1,069.5 eV. This peak represents sodium perchlorate, which is associated with the electrolyte used to fabricate the cell and form a solid electrolyte interphase (SEI) layer.[24] The XPS analysis of these anodes confirms the successful formation of a SEI layer. However, a quantitative analysis of Na elements was difficult to perform because the charging process cannot completely transfer Na ions from the working anode. Nonetheless, the N 1s XPS spectrum of O-pNaPc anode in charged state shows evident

disappearance of N2 peak, which indicates the removal of Na ions from the Pc core (**Figure S10**). This result supports our assumption that Pc core acts as the storage sites for Na ions.

The transfer of Na ions can be identified by Raman spectra of the anode samples used for the XPS analysis. The Raman bands for the analysis were carefully selected by comparing the Raman spectra of commercial NaPc and H_2Pc (**Figure S11**), which indicate that B_{2g} and B_{1g} bands at *ca.* 1,430 and 1,510 cm^{-1}, respectively, are evident in the presence of Na ions. Despite the slight shift owing to the chemical differences, O- and S-*p*NaPcs display strong B_{2g} and B_{1g} bands that represent the interactions with Na ions (**Figure 2c**). Thus, we infer that these bands are associated with the coordination of the Na ions with the Pc core. In **Figure 4c**, the Raman spectrum of the pristine O-*p*NaPc anode shows relatively weak yet discernible B_{2g} (1,403 cm^{-1}) and B_{1g} (1,528 cm^{-1}) bands. These B_{2g} and B_{1g} bands intensify after the discharging and diminish after the charging process. The substantial difference in band intensity after charging and discharging is ascribable to the coordination and dissociation of Na ions with the Pc core, as demonstrated by the comparable Raman spectra of NaPc and H_2Pc. The variation in Raman intensities of O-*p*NaPc electrode was visualized by the Raman mapping images taken at different charge states for an area of 10 x 10 μm^2 (**Figure 4d**). The intensities of the characteristic B_{2g} and B_{1g} bands are compared with those of carbon D (1,320 cm^{-1}) and G (1,594 cm^{-1}) bands and their intensity ratio $I_{(B1g+B2g)}/I_{(D+G)}$ is expressed by the RGB color scale. The D and G bands are chosen as the reference since they show no intensity changes during the charging/discharging process. A larger red area, which indicates a high concentration of Na ions, is observed in the discharged sample. In contrast, white and blue, which indicate low Na ion concentrations, are dominant in the charged sample. These results confirm that the Na ions in O-*p*NaPc can reversibly coordinate with/dissociate from Pc moiety during cycling.

We then fabricated SIB anodes using O-*p*NaPc, S-*p*NaPc, and the commercial NaPc to examine their electrochemical properties. The effect of the linkers was first investigated by

cyclic voltammetry (CV) at a scan rate of 0.1 mV s^{-1} in a potential window from 0.01 to 2.0 V (**Figure 5a**). Both *p*NaPc anodes exhibit CVs that are similar in shape to that of typical carbon anodes of SIBs, and their reduction and oxidation peaks appear at *ca.* 0.7 and 0.3 V *vs.* Na/Na^+, respectively. It is notable that the O-*p*NaPc anode exhibits a lower oxidation potential than the S-*p*NaPc anode (by 35.3 mV, inset of **Figure 5a**), which is ascribable to the weaker binding energy of Na ions to the Pc core of the O-*p*NaPc. This finding is in good agreement with the DFT calculations and the XPS analyses. Compared with the *p*NaPc anodes, the NaPc anode has a much lower oxidation potential, which confirms the absence of electron-donating groups and thus a weaker binding energy between the Na ions and the Pc core.

The galvanostatic profiles of *p*NaPc and NaPc anodes at a current density of 0.1 A g^{-1} in the potential window from 0.01 to 2.0 V are shown in **Figure 5b**. In the discharge profiles of the first cycle, the O- and S-*p*NaPc anodes display similar specific capacities of 610.2 and 606.2 mA h g^{-1}, respectively. In the charge profiles, they exhibit slightly different capacities of 140.7 and 130.9 mA h g^{-1}, respectively. The O-*p*NaPc anode has specific capacities of 164.8 and 138.4 mA h g^{-1} in the discharge and charge profiles of the second cycle, respectively, revealing that it has better reversibility than the S-*p*NaPc anode (153.9 and 126.6 mA h g^{-1}, respectively). This difference can be attributed to the desirable Na–N binding energy in O-*p*NaPc (Table S1) resulting from the less favorable electronic structure hybridization between Na and N (**Figure 3b**). Conversely, the NaPc anode had a similar initial specific capacity of 618.1 mA h g^{-1} in the first discharge profile but a very low specific capacity of 77.8 mA h g^{-1} in the first charge profile because of its structural instability, which corresponds with the low oxidation potential of the NaPc anode. The galvanostatic profiles conducted at a current density of 0.2 A g^{-1} after the 200th cycle are also indicative of the good cycling stabilities of the O- and S-*p*NaPc anodes (**Figure S12**). This is particularly apparent in the 200th cycle, where the O- and S-*p*NaPc anodes had specific capacities of 103.8 and 97.9 mA h g^{-1} in the discharge profiles, and 102.6 and 97.2 mA h g^{-1} in the charge profiles,

respectively. Due to the typical irreversibility of the conducting agent (Super P), the O-*p*NaPc and S-*p*NaPc anodes have low initial Coulombic efficiencies of 19.8 and 18.0 %, which dramatically increase to 82.8 and 80.9 %, 95.9 and 89.2 %, and 98.8 and 99.3 % in the 2nd, 10th, and 200th cycles, respectively. This excellent capacity retention can be attributed to the superior reversibility of the Na ions between the *p*NaPcs and Na metal during cycling.

The rate capacities of *p*NaPc and NaPc anodes were evaluated at various current densities per 10 cycles (**Figure 5c**). The O-*p*NaPc anode delivers 145.1, 109.8, 81.5, 68.9, 62.0, and 56.9 mA h g^{-1} at the current densities of 0.1, 0.2, 0.5, 1.0, 1.5, and 2.0 A g^{-1}, respectively, showing a slightly better rate performance than the S-*p*NaPc anode. Upon returning to a current density of 0.1 A g^{-1}, the O-*p*NaPc anode recovers a specific capacity of 136.7 mA h g^{-1}, demonstrating excellent rate capability and reversibility in the SIB application. Such excellent performances of O-*p*NaPc arise from the good thermal and physicochemical stability of polymeric Pcs and the stable interaction between the isoindolic N and Na ions. In contrast, the NaPc anode performs poorly in terms of rate capability and other electrochemical performance parameters, showing severe capacity fading to a capacity near 0 mA g^{-1} at a current density of 1.0 A g^{-1}. As stated earlier, the instability of the NaPc anode results from the electrochemical nature of the compound and its intrinsic solubility in the electrolyte. **Figure 5d** shows the pristine NaPc and O-*p*NaPc anodes immersed in the electrolyte (1 M $NaClO_4$ in 1:1 v/v mixture of EC and propylene carbonate) and the visual observation of their cycled electrodes. The initially colorless electrolyte rapidly turns blue due to NaPc dissolution, while the color of the electrolyte containing the O-*p*NaPc anode remains unchanged after 10 min. These results demonstrate the enhanced structural stability of polymeric compounds, which may positively affect the reversibility of *p*NaPcs with stable cyclability and high capacity under a high current density. The photographic images in **Figure 5d** reveal that the surface of NaPc anode is severely damaged and shows the partial detachment of active

materials after cycling, whereas the cycled O-*p*NaPc and S-*p*NaPc electrodes (**Figure 5d** and **S13**, respectively) show almost intact surfaces without much degradation.

Consistently, in the cycle performance test at a current density of 0.2 A g^{-1} (**Figure 5e**), both *p*NaPc anodes deliver superior specific capacities and cycle stabilities for 200 cycles compared with the NaPc anode. The O- and S-*p*NaPc anodes deliver the initial discharge capacities of 556.9 and 539.4 mA h g^{-1} with Coulombic efficiencies of 18.0 and 19.8 % in the first cycles and 96.2 and 97.2 % after 20 cycles, respectively. The O- and S-*p*NaPc anodes show excellent cycle stabilities, delivering specific capacities of 96.0 and 94.6 mA h g^{-1} after 200 cycles. However, the NaPc anode suffers unstable cyclability with severe capacity fading and fails after 50 cycles. These results demonstrate that the polymerization strategy we applied to overcome the structural instability and disadvantages of the NaPc monomer significantly improves the structural stability of the organic anodes and prevents their dissolution into the electrolyte. The reversibility of the redox reaction at O- and S-*p*NaPc anode was investigated by conducting CV analysis at various scan rates (**Figure S14**). At scan rates from 0.1 to 1.0 mV s^{-1}, O-*p*NaPc anode shows a redox peak couple whose position remains almost unchanged, indicating its fast electrochemical kinetics. The redox kinetics of *p*NaPc anodes was further compared using electrochemical impedance spectroscopy (EIS, **Figure S15**). The fresh O-*p*NaPc anode shows a charge transfer resistance (R_{ct}) of 530.2 ± 0.2 Ω, which is lower than that of S-*p*NaPc (580.2 ± 0.2 Ω). The O-*p*NaPc anode cycled for 200 cycles also shows a lower R_{ct} value (390.2 ± 0.2 Ω) than the S-*p*NaPc anode (420.2 ± 0.2 Ω), which confirms the improved redox kinetics thanks to the weaker binding energy of the O linker.

Inspired by the excellent electrochemical performances of O-*p*NaPc anode, we fabricated a Na-ion full cell using the discharged O-*p*NaPc anode against the previously reported NVPF/C cathode at a voltage window from 1.0 to 4.0 V (**Figure 5f**).[27] The XRD pattern of the NVPF/C presented in **Figure S16** matches well with the previous report.[22] Prior to

fabricating the full cell, the O-*p*NaPc anode was galvanostatically cycled twice between 0.01 and 3.0 V in the half-cell (*i.e.*, *vs.* Na/Na^+) at the current density of 50 mA g^{-1} and then discharged to a cut-off voltage of 0.01 V. In accordance with the principle of balanced charge transfer through the anode and cathode, the negative/positive capacity ratio was maintained below 1.2. This value is based on the NVPF/C and O-*p*NaPc capacities of 128 and 120 mA h g^{-1}, respectively. **Figure 5g** shows the charge and discharge cycle profiles of the full cell for 1, 2, 5, 10, 15, 20, and 30 cycles at the current density of 50 mA g^{-1}. The characteristic plateau corresponding to the sodiation and desodiation processes of the as-prepared NVPF/C cathode can be observed. The full cell shows a high specific discharge capacity of 106.7 mA h g^{-1} at a current density of 0.1 A g^{-1} and good stability for up to 30 cycles with high Coulombic efficiency (**Figure 5h**). Our full cell delivers an energy density of 288 Wh kg^{-1} and a power density of 149 W kg^{-1}, and demonstrates great potential of organic anodes for practical application in the next-generation SIBs.

3. Conclusion

In summary, polymeric disodium phthalocyanines with O and S linkers, namely O-*p*NaPc and S-*p*NaPc, were successfully synthesized and applied as anodes in SIBs. These compounds were thoroughly characterized using various microscopic and spectroscopic analytical methods. O-*p*NaPc and S-*p*NaPc showed similar FT-IR and Raman spectra but different UV–vis spectra and XPS profiles due to the different peripheral substituents. The peak shifts in the XPS analysis revealed the weaker binding energy between the Na ion and the isoindolic N of the O-*p*NaPc cores. This result was further supported by the DFT calculations that revealed the weaker adsorption energy associated with the interaction of the Na ions with the Pc core of O-*p*NaPc compared with that associated with the interaction of the Na ions with the Pc core of S-*p*NaPc. As suggested by the XPS analysis and the DFT calculation results, the electrochemical performance of the O-*p*NaPc anode in SIB was superior to that of the S-

*p*NaPc anode, in terms of stability and reversibility, and the O-*p*NaPc anode SIB delivered 56.9 mA h g^{-1} at a high current density (2.0 A g^{-1}) and retained 97.9 mA h g^{-1} after 200 cycles. This work illustrates that polymeric phthalocyanines are a promising platform for various types of anodes in energy conversion and storage applications, and their performance can be fine-tuned by changing the linkers of the Pc units.

4. Experimental Section

Chemicals: Dichlorobenzene was freshly distilled before use. 1-Pentanol was distilled from Na under reduced pressure. Toluene, *N*,*N*-dimethylformamide (DMF), and dichloromethane (DCM) were purified using a PureSolv solvent purification system (Inert Corp., USA). 4-Nitrophthalonitrile (99 %), 1,3-propanediol (98 %), 1,3-propanedithiol (99 %), potassium carbonate (anhydrous, 99.9 %), sodium metal (Na metal, 99.9 % in mineral oil), *N*-methyl-2-pyrrolidinone (≥ 99.5 %), ethylene carbonate (EC, anhydrous, ≥ 99 %), diethylcarbonate (DEC, anhydrous, ≥99 %), sodium perchlorate ($NaClO_4$, 98 %), fluoroethylene carbonate (FEC, anhydrous, ≥ 99 %), vanadium pentoxide (99.95 %), oxalic acid (*ReagentPlus*®, ≥ 99 %), ammonium dihydrogen phosphate (99.99 %), sodium fluoride (99 %), graphene oxide (0.5 wt.% in H_2O), and ammonium hydroxide (ACS reagent, 28.0–30.0 % NH_3 basis) were purchased from Sigma–Aldrich and used as received.

Instrumentation: All reactions were performed under an inert atmosphere of dry N_2 or Ar gas and monitored by thin-layer chromatography on Merck pre-coated silica gel 60 F_{254} aluminium plates. Chromatographic purification was performed on a silica gel (Macherey-Nagel, 230–400 mesh) column with the indicated eluents. ^1H and $^{13}C\{^1H\}$ NMR spectra were recorded on a Bruker AVANCE III 400 MHz spectrometer (^1H 400 MHz; ^{13}C 100.6 MHz) in DMSO-d_6. Electrospray ionization (ESI) mass spectra were collected on a Thermo Finnigan MAT 95 XL mass spectrometer. Sample morphology and structure were investigated by scanning electron microscopy (SEM; TESCAN VEGA3) and high-resolution transmission

electron microscopy (HRTEM; JEOL JEM-2100F). A suspension of O- and S-*p*NaPcs in ethanol (*ca.* 0.05 mg mL^{-1}) was drop-cast on a carbon-coated Cu grid for HRTEM analysis. The samples were fully dried before characterization. During the imaging process, no structural changes were observed at the operating voltage (200 kV). Electronic absorption spectra were acquired on a Cary 5G ultraviolet-visible-near-infrared (UV–vis–NIR) spectrophotometer. Fourier-transform infrared (FT-IR) spectroscopy was performed between 4,000 and 400 cm^{-1} using a Thermo Nicolet iS 10 mid-FTIR spectrometer. X-ray photoelectron spectroscopy (XPS) was performed using a Thermo Fisher ESCALAB 250Xi system. The spectrometer was calibrated using the C 1s peak at 284.3 eV, and data were fitted with XPS 41 software. Raman spectra were acquired using a WITec confocal Raman system (alpha300 R). An excitation laser (λ = 532 nm) with a power of 5 mW was used for all the tests to minimize the heat damage to the samples.

Preparation of O-Pn dimer: 4-Nitrophthalonitrile (2.00 g, 11.6 mmol) and 1,3-propanediol (0.35 g, 4.6 mmol) were dissolved in DMF (10 mL) and treated with potassium carbonate (3.19 g, 23.1 mmol). The resulting mixture was stirred at 50 °C for 72 h. Deionized (DI) water (200 mL, Milli-Q system) was then added under continuous stirring, and the resulting mixture was stirred at room temperature for 1 h. The precipitate formed was collected by filtration and washed successively with DI water (200 mL) and MeOH (200 mL). The solid was dissolved in DCM (20 mL) and purified by column chromatography on silica gel, eluting with DCM to yield the product as a white powder (1.20 g, 79 %). ^{1}H NMR (400 MHz, DMSO-d_6): δ 8.02 (d, J = 8.8 Hz, 2 H, ArH), 7.75 (d, J = 2.4 Hz, 2 H, ArH), 7.45 (dd, J = 2.4, 8.8 Hz, 2 H, ArH), 4.30 (t, J = 6.0 Hz, 4 H, OCH_2), 2.24 (q, J = 6.0 Hz, 2 H, CH_2). $^{13}C\{^{1}H\}$ NMR (100.6 MHz, DMSO-d_6): δ 161.7, 135.8, 120.3, 120.1, 116.3, 116.2, 115.7, 106.0, 65.6, 27.8. HRMS (ESI): m/z calcd. for $C_{19}H_{12}N_4NaO_2$ $[M+Na]^+$, 351.0852; found, 351.0850.

Preparation of S-Pn dimer: The S-Pn dimer was prepared using a similar method. 4-Nitrophthalonitrile (2.00 g, 11.6 mmol) and 1,3-propanedithiol (0.50 g, 4.6 mmol) were

dissolved in DMF (10 mL) followed by the addition of potassium carbonate (3.19 g, 23.1 mmol). By the same procedure described above, the precipitate was collected and recrystallized from hot MeOH to yield the product as an ivory powder (1.60 g, 96 %). ^{1}H NMR (400 MHz, DMSO-d_6): δ 8.03 (s, 2 H, ArH), 7.97 (d, J = 8.4 Hz, 2 H, ArH), 7.76 (d, J = 8.4 Hz, 2 H, ArH), 3.27 (t, J = 7.2 Hz, 4 H, SCH_2), 1.95 (quintet, J = 7.2 Hz, 2 H, CH_2). ^{13}C{^{1}H} NMR (100.6 MHz, DMSO-d_6): δ 145.9, 133.7, 130.5, 130.3, 116.1, 115.6, 115.2, 109.9, 29.2, 27.0. HRMS (ESI): *m/z* calcd. for $C_{19}H_{12}N_4NaS_2$ $[M + Na]^+$, 383.0396; found, 383.0395.

Electrochemical measurements: To fabricate an anode, a slurry containing the as-prepared *p*NaPc, a conducting agent (Super P), and a binder (polyvinylidene difluoride) in a weight ratio of 4:5:1 was prepared in *N*-methyl-2-pyrrolidinone and mixed using a ball-mill (Mini-Mill PULVERISETTE 23, FRITSCH). The slurry was cast onto clean copper foil using a doctor blade and then dried in a vacuum oven at 70 °C overnight. The anode was cut to a 12-mm diameter, and the average mass loading of the active materials was 1.1 mg cm^{-2}. Electrochemical tests were conducted with a coin-type cell (CR 2016) configuration using Na metal as the counter electrode and a glass fiber separator (Whatman GF/C). A mixed solvent of EC and DEC (1:1 by weight) containing $NaClO_4$ (1 M) and FEC additive (1 wt.%) was used as the electrolyte. The electrolyte concentration was set to 30 μL mg^{-1} for all tests. Coin cells were assembled in an Ar-filled glovebox (H_2O and O_2 < 0.1 ppm). All electrochemical tests were conducted using a WBCS3000S cycler (WonATech Co.) at various current densities in a voltage range from 0.01 to 2.0 V (*vs.* Na/Na^+). Cyclic voltammetry (CV) was performed between 0.01 and 2.0 V (*vs.* Na/Na^+) at various scan rates from 0.1 to 1.0 mV s^{-1}. Electrochemical impedance spectroscopy (EIS) was conducted using a PARSTAT MC (PMC1000/DC) electrochemical system (Princeton Applied Research, USA) in a frequency range between 0.1 and 100 kHz.

Preparation of the NVPF/C material: NVPF/C was prepared as previously reported[29] with minor modifications. In a typical preparation, vanadium pentoxide (364 mg) and oxalic acid (648 mg) in a molar ratio of 1:3 were dissolved in DI water (30 mL) and stirred at 70 °C for 30 min. The solution was treated with ammonium dihydrogen phosphate (460 mg) and sodium fluoride (252 mg). The mixture was then stirred for another 30 min before graphene oxide (12 mL; 0.5 wt.% in H_2O) was added. The pH was adjusted to 7.0 using ammonium hydroxide, and then the solution was stirred for 2 h. The reaction mixture was subsequently transferred to a Teflon-lined autoclave reactor and then heated at 170 °C for 12 h. After cooling down to room temperature, the crude product was collected, centrifuged, and washed thoroughly with DI water and ethanol. The obtained powder was dried at 80 °C overnight and then annealed at 500 °C for 4 h with a ramping rate of 5 °C min^{-1} under an Ar atmosphere to afford the final product as a dark grey powder.

Computational simulations: First-principles DFT calculations were performed using the projector-augmented wave method[30] within the Vienna *ab initio* Simulation Package.[31] The generalized gradient approximation was implemented with Perdew–Burke–Ernzerhof[32] parameterization to describe the exchange-correlation functional. The kinetic energy cut-off was set to 520 eV, and the energy and force convergence criteria were 10^{-5} eV and 0.02 eV $Å^{-1}$, respectively. The Brillouin zone was sampled with a gamma-centered 3 × 3 × 1 *k*-point grid for optimizing the *p*NaPcs, whereas a 19 × 19 × 19 *k*-point scheme was applied to the bulk Na. The van der Waals interaction was corrected *via* Grimme's DFT-D3 method.[33] Each unit cell contained one *p*NaPc unit separated by 20 Å of vacuum space perpendicular to the *p*NaPc plane.

Supporting Information

Supporting Information (SI) is available from the Wiley Online Library or from the author.

SI includes NMR spectra, SEM images, XPS spectra, HOMO–LUMO energy diagram, Raman spectra, Galvanostatic discharge/charge profiles, CV analysis, and EIS spectra, XRD patterns, and binding energy images with Na-ion.

Acknowledgements

The authors gratefully acknowledge the financial supports from the Research Grants Council of the Hong Kong Special Administrative Region (PolyU15217521), the Hong Kong Polytechnic University (Q-CDA3), and Initiative for fostering University of Research and Innovation Program of the National Research Foundation (NRF) funded by the Korean government (MSIT) (No.2020M3H1A1077095). YK and DK also acknowledge the award of Hong Kong Ph.D. Fellowship.

Received: ((will be filled in by the editorial staff))
Revised: ((will be filled in by the editorial staff))
Published online: ((will be filled in by the editorial staff))

References

[1] T. Liu, Y. Zhang, Z. Jiang, X. Zeng, J. Ji, Z. Li, X. Gao, M. Sun, Z. Lin, M. Ling, J. Zheng, C. Liang, *Energy Environ. Sci.* **2019**, *12*, 1512-1533.

[2] F. Duffner, N. Kronemeyer, J. Tübke, J. Leker, M. Winter, R. Schmuch, *Nat. Energy* **2021**, *6*, 123-134.

[3] a) C. Yang, S. Xin, L. Mai, Y. You, *Adv. Energy Mater.* **2021**, *11*, 2000974; b) J.-Y. Hwang, S.-T. Myung, Y.-K. Sun, *Chem. Soc. Rev.* **2017**, *46*, 3529; c) Z. Zhang, Y. Du, Q. C. Wang, J. Xu, Y. N. Zhou, J. Bao, J. Shen, X. Zhou, *Angew. Chem. Int. Ed.* **2020**, *59*, 17504-17510; d) E. Gu, S. Liu, Z. Zhang, Y. Fang, X. Zhou, J. Bao, *J. Alloys Compd.* **2018**, *767*, 131-140; e) J. Xu, Y. Xu, C. Lai, T. Xia, B. Zhang, X. Zhou, *Sci. China Chem.* **2021**, *64*, 1267-1282.

[4] a) S. Liang, Y.-J. Cheng, J. Zhu, Y. Xia, P. Müller-Buschbaum, *Small Methods* **2020**, *4*, 2000218; b) J. Li, W. Qin, J. Xie, R. Lin, Z. Wang, L. Pan, W. Mai, *Chem. Eng. J.* **2018**, *332*, 260-266; c) J. Li, Z. Ding, L. Pan, J. Li, C. Wang, G. Wang, *Carbon* **2021**, *173*, 31-40; d) J. Li, Z. Ding, J. Li, C. Wang, L. Pan, G. Wang, *Chem. Eng. J.* **2021**, *407*, 127199.

[5] a) D. P. DiVincenzo, E. J. Mele, *Phys. Rev. B*, **1985**, *32*, 2538-2553; b) Y. Matsuo, K. Hashiguchi, K. Ueda, Y. Muramatsu, *Electrochem.* **2015**, *83*, 345-347.

[6] a) J. J. Shea, C. Luo, *ACS Appl. Mater. Interfaces* **2020**, *12*, 5361-5380; b) J. Heiska, M. Nisula, M. Karppinen, *J. Mater. Chem. A* **2019**, *7*, 18735-18758; c) M. Yu, N. Chandrasekhar, R. K. M. Raghupathy, K. H. Ly, H. Zhang, E. Dmitrieva, C. Liang, X. Lu, T. D. Kühne, H. Mirhosseini, I. M. Weidinger, X. Feng, *J. Am. Chem. Soc.* **2020**, *142*, 19570-19578; d) X. X. Luo, W. H. Li, H. J. Liang, H. X. Zhang, K. D. Du, X. T. Wang, X. F. Liu, J. P. Zhang, X. L. Wu, *Angew. Chem. Int. Ed.* **2022**, *61*, e202117661.

[7] Y. Xu, M. Zhou, Y. Lei, *Mater. Today* **2018**, *21*, 60-78.

[8] a) L. Zhao, J. Zhao, Y.-S. Hu, H. Li, Z. Zhou, M. Armand, L. Chen, *Adv. Energy Mater.* **2012**, *2*, 962-965; b) Y. Park, D.-S. Shin, S. H. Woo, N. S. Choi, K. H. Shin, S. M. Oh, K. T. Lee, S. Y. Hong, *Adv. Mater.* **2012**, *24*, 3562-3567; c) A. Abouimrane, W. Weng, H. Eltayeb, Y. Cui, J. Niklas, O. Poluektov, K. Amine, *Energy Environ. Sci.* **2012**, *5*, 9632-9638.

[9] a) S. Gu, S. Wu, L. Cao, M. Li, N. Qin, J. Zhu, Z. Wang, Y. Li, Z. Li, J. Chen, Z. Lu, *J. Am. Chem. Soc.* **2019**, *141*, 9623-9628; b) K. Sakaushi, E. Hosono, G. Nickerl, T. Gemming, H. Zhou, S. Kaskel, J. Eckert, *Nat. Commun.* **2013**, *4*, 1485; c) S. Wu, W. Wang, M. Li, L. Cao, F. Lyu, M. Yang, Z. Wang, Y. Shi, B. Nan, S. Yu, Z. Sun, Y. Liu,

Z. Lu, *Nat. Commun.* **2016**, *7*, 13318; d) H. Duan, P. Lyu, J. Liu, Y. Zhao, Y. Xu, *ACS Nano* **2019**, *13*, 2473-2480; e) J. He, N. Wang, Z. Cui, H. Du, L. Fu, C. Huang, Z. Yang, X. Shen, Y. Yi, Z. Tu, Y. Li, *Nat. Commun.* **2017**, *8*, 1172.

[10] S. Eder, D.-J. Yoo, W. Nogala, M. Pletzer, A. Santana Bonilla, A. J. P. White, K. E. Jelfs, M. Heeney, J. W. Choi, F. Glöcklhofer, *Angew. Chem. Int. Ed.* **2020**, *59*, 12958-12964.

[11] a) K. Chen, K. Liu, P. An, H. Li, Y. Lin, J. Hu, C. Jia, J. Fu, H. Li, H. Liu, Z. Lin, W. Li, J. Li, Y.-R. Lu, T.-S. Chan, N. Zhang, M. Liu, *Nat. Commun.* **2020**, *11*, 4173; b) S. Wei, H. Zou, W. Rong, F. Zhang, Y. Ji, L. Duan, *Appl. Catal. B Environ.* **2021**, *284*, 119739; c) Z. Yue, C. Ou, N. Ding, L. Tao, J. Zhao, J. Chen, *ChemCatChem* **2020**, *12*, 6103-6130.

[12] T. Furuyama, K. Satoh, T. Kushiya, N. Kobayashi, *J. Am. Chem. Soc.* **2014**, *136*, 765-776.

[13] a) N. Han, Y. Wang, L. Ma, J. Wen, J. Li, H. Zheng, K. Nie, X. Wang, F. Zhao, Y. Li, J. Fan, J. Zhong, T. Wu, D. J. Miller, J. Lu, S.-T. Lee, Y. Li, *Chem* **2017**, *3*, 652-664; b) S. Aralekallu, I. Mohammed, N. Manjunatha, M. Palanna, Dhanjai, L. K. Sannegowda, *Sens. Actuators B Chem.* **2019**, *282*, 417-425; c) W.-Z. Cheng, J.-L. Liang, H.-B. Yin, Y.-J. Wang, W.-F. Yan, J.-N. Zhang, *Rare Met.* **2020**, *39*, 815-823; d) D. Qi, X. Chen, W. Liu, C. Liu, W. Liu, K. Wang, J. Jiang, *Inorg. Chem. Front.* **2020**, *7*, 642-646.

[14] Y. Kim, D. Kim, J. Lee, L. Y. S. Lee, D. K. Ng, *Adv. Funct. Mater.* **2021**, *31*, 2103290.

[15] a) K. Nakai, J. Usami, N. Kobayashi, *J. Porphyr. Phthalocya.* **2007**, *11*, 222-227; b) K. S. Lokesh, N. Uma, B. N. Achar, *J. Non-Cryst. Solids* **2007**, *353*, 384-389.

[16] D. Wöhrle, E. Preußner, *Macromol. Chem. Phys.* **1985**, *186*, 2189-2207.

[17] a) J. Su, J.-J. Zhang, J. Chen, Y. Song, L. Huang, M. Zhu, B. I. Yakobson, B. Z. Tang, R. Ye, *Energy Environ. Sci.* **2021**, *14*, 483-492; b) P. Alessio, M. L. Rodríguez-Méndez, J. A. De Saja Saez, C. J. L. Constantino, *Phys. Chem. Chem. Phys.* **2010**, *12*, 3972-3983.

[18] X. Hu, S. Zhang, J. Sun, L. Yu, X. Qian, R. Hu, Y. Wang, H. Zhao, J. Zhu, *Nano Energy* **2019**, *56*, 109-117.

[19] a) Z. Wu, L.-P. Sun, M. Yang, L.-H. Huo, H. Zhao, J.-C. Grenier, *J. Mater. Chem. A* **2016**, *4*, 13534-13542; b) J. V. Rojas, M. Toro-Gonzalez, M. C. Molina-Higgins, C. E. Castano, *Mater. Sci. Eng. B* **2016**, *205*, 28-35.

[20] B. V. R. Reddy, R. Ravikumar, C. Nithya, S. Gopukumar, *J. Mater. Chem. A* **2015**, *3*, 18059-18063.

[21] L. Qie, W. Chen, X. Xiong, C. Hu, F. Zou, P. Hu, Y. Huang, *Adv. Sci.* **2015**, *2*, 1500195.

[22] a) W. Gu, M. Sevilla, A. Magasinski, A. B. Fuertes and G. Yushin, *Energy Environ. Sci.*, 2013, **6**, 2465-2476; b) D. G. d. Oteyza, A. El-Sayed, J. M. Garcia-Lastra, E. Goiri, T. N. Krauss, A. Turak, E. Barrena, H. Dosch, J. Zegenhagen, A. Rubio, Y. Wakayama, J. E. Ortega, *J. Chem. Phys.* **2010**, *133*, 214703; c) M. Wang, J. Han, Y. Hu, R. Guo, *RSC Adv.* **2017**, *7*, 15513-15520.

[23] a) Y. Wang, N. Hu, Z. Zhou, D. Xu, Z. Wang, Z. Yang, H. Wei, E. S.-W. Kong, Y. Zhang, *J. Mater. Chem.* **2011**, *21*, 3779-3787; b) Y. Xia, S. Kashtanov, P. Yu, L.-Y. Chang, K. Feng, J. Zhong, J. Guo, X. Sun, *Nano Energy* **2020**, *67*, 104163; c) I. S. Kwon, I. H. Kwak, J. Y. Kim, H. G. Abbas, T. T. Debela, J. Seo, M. K. Cho, J.-P. Ahn, J. Park, H. S. Kang, *Nanoscale* **2019**, *11*, 14266-14275.

[24] a) A. Cano, L. Lartundo-Rojas, A. Shchukarev, E. Reguera, *New J. Chem.* **2019**, *43*, 4835-4848; b) K. Artyushkova, B. Kiefer, B. Halevi, A. Knop-Gericke, R. Schlogl, P. Atanassov, *Chem. Commun.* **2013**, *49*, 2539-2541.

[25] C. G. Claessens, U. Hahn, T. Torres, *Chem. Rec.* **2008**, *8*, 75-97.

[26] I. Moeez, H. D. Lim, J. H. Park, H. G. Jung, K. Y. Chung, *ACS Energy Lett.* **2019**, *4*, 2060-2068.

[27] a) S. Liu, X. Cao, Y. Zhang, K. Wang, Q. Su, J. Chen, Q. He, S. Liang, G. Cao, A. Pan, *J. Mater. Chem. A* **2020**, *8*, 18872-18879; b) C. Wang, D. Du, M. Song, Y. Wang, F. Li, *Adv. Energy Mater.* **2019**, *9*, 1900022.

[28] a) J. Z. Guo, P. F. Wang, X. L. Wu, X. H. Zhang, Q. Yan, H. Chen, J. P. Zhang, Y. G. Guo, Adv. Mater. **2017**, *29*, 1701968; b) Y. Cai, X. Cao, Z. Luo, G. Fang, F. Liu, J. Zhou, A. Pan, S. Liang, *Adv. Sci.* **2018**, *5*, 1800680.

[29] J. Z. Guo, P. F. Wang, X. L. Wu, X. H. Zhang, Q. Yan, Chen, H., J.-P. Zhang, Y. G. Guo, *Adv. Mater.*, **2017**, *29*, 1701968.

[30] P. E. Blöchl, *Phys. Rev. B*, **1994**, *50*, 17953.

[31] G. Kresse, J. Furthmüller, *Phys. Rev. B*, **1996**, *54*, 11169.

[32] J. P. Perdew, A. Ruzsinszky, G. I. Csonka, O. A. Vydrov, G. E. Scuseria, L. A. Constantin, X. Zhou, K. Burke, *Phys. Rev. Lett.*, **2008**, *100*, 136406.

[33] S. Grimme, J. Antony, S. Ehrlich, H. Krieg, *J. Chem. Phys.*, **2010**, *132*, 154104.

List of figures

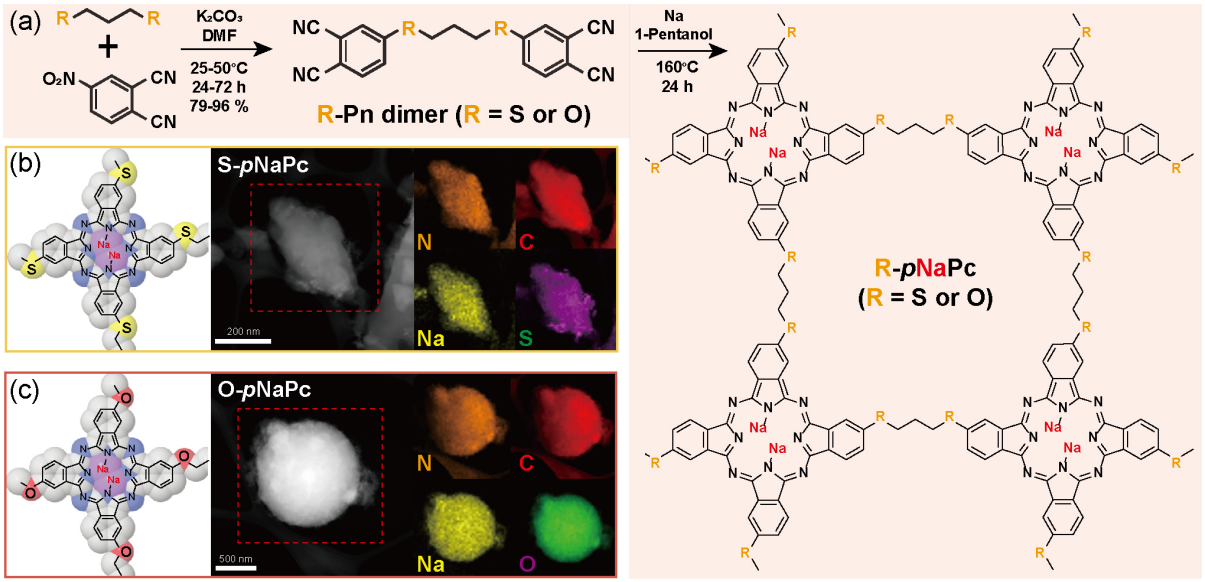

Figure 1. (a) Schematic illustration of the synthesis of polymeric disodium phthalocyanines (*p*NaPcs). Proposed structures and TEM images of (b) S-*p*NaPc and (c) O-*p*NaPc with the corresponding EDX mapping images.

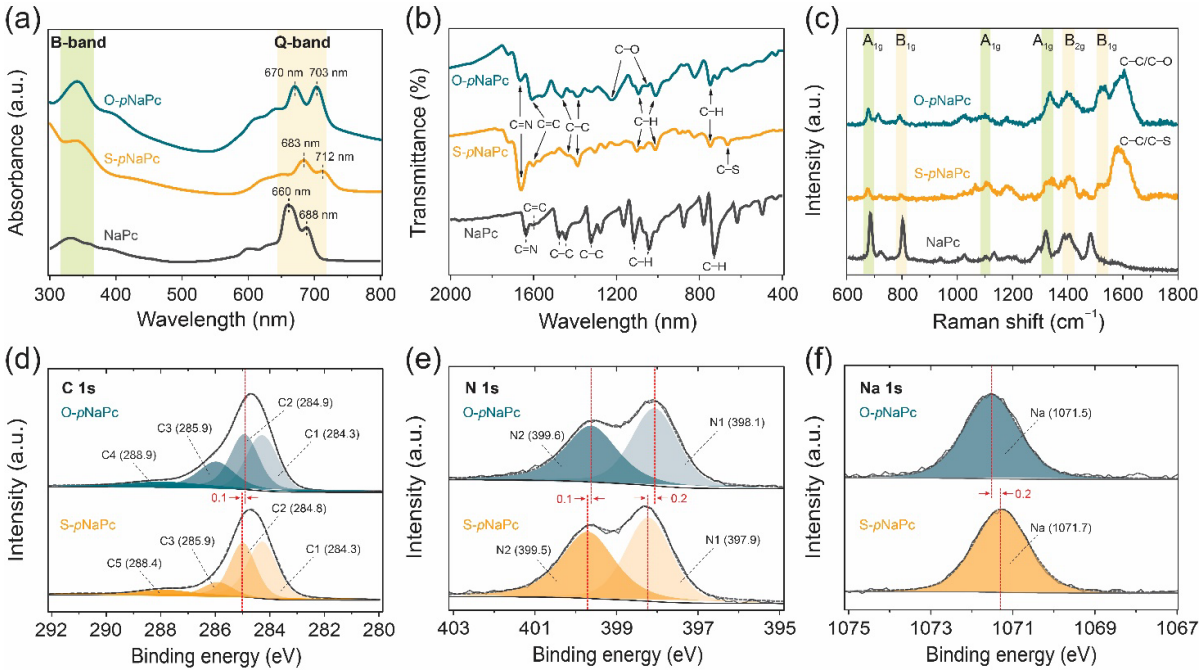

Figure 2. (a) UV–vis, (b) Raman, and (c) FT-IR spectra of O-*p*NaPc, S-*p*NaPc, and NaPc. High-resolution XPS spectra of pNaPcs in (d) C 1s, (e) N 1s, and (f) Na 1s regions.

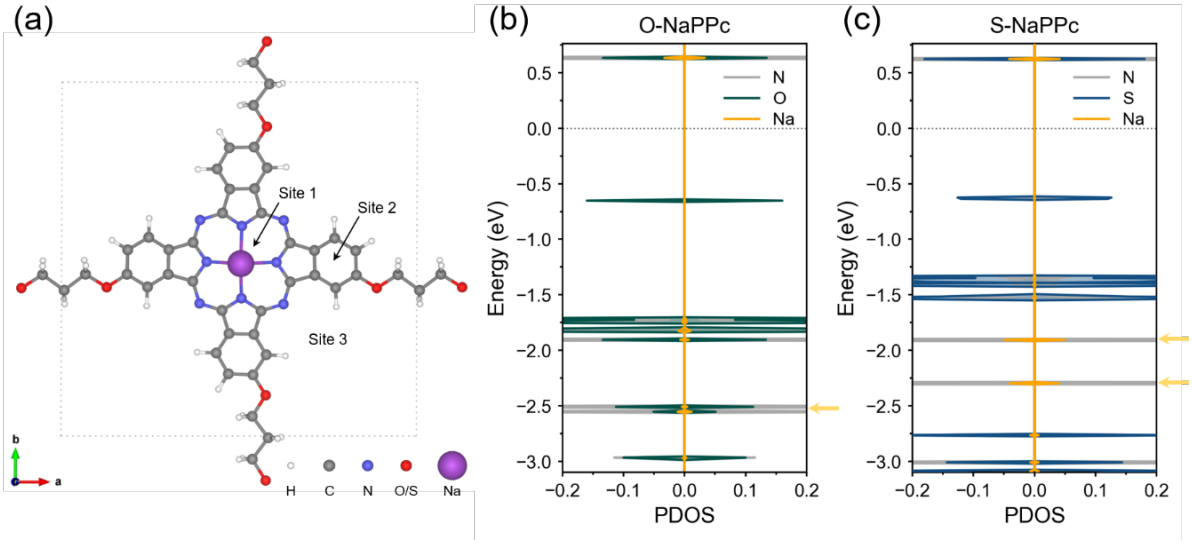

Figure 3. (a) Model system of O/S-*p*NaPc. PDOS of (b) O-*p*NaPc and (c) S-*p*NaPc. Yellow arrows indicate the prominent Na peaks.

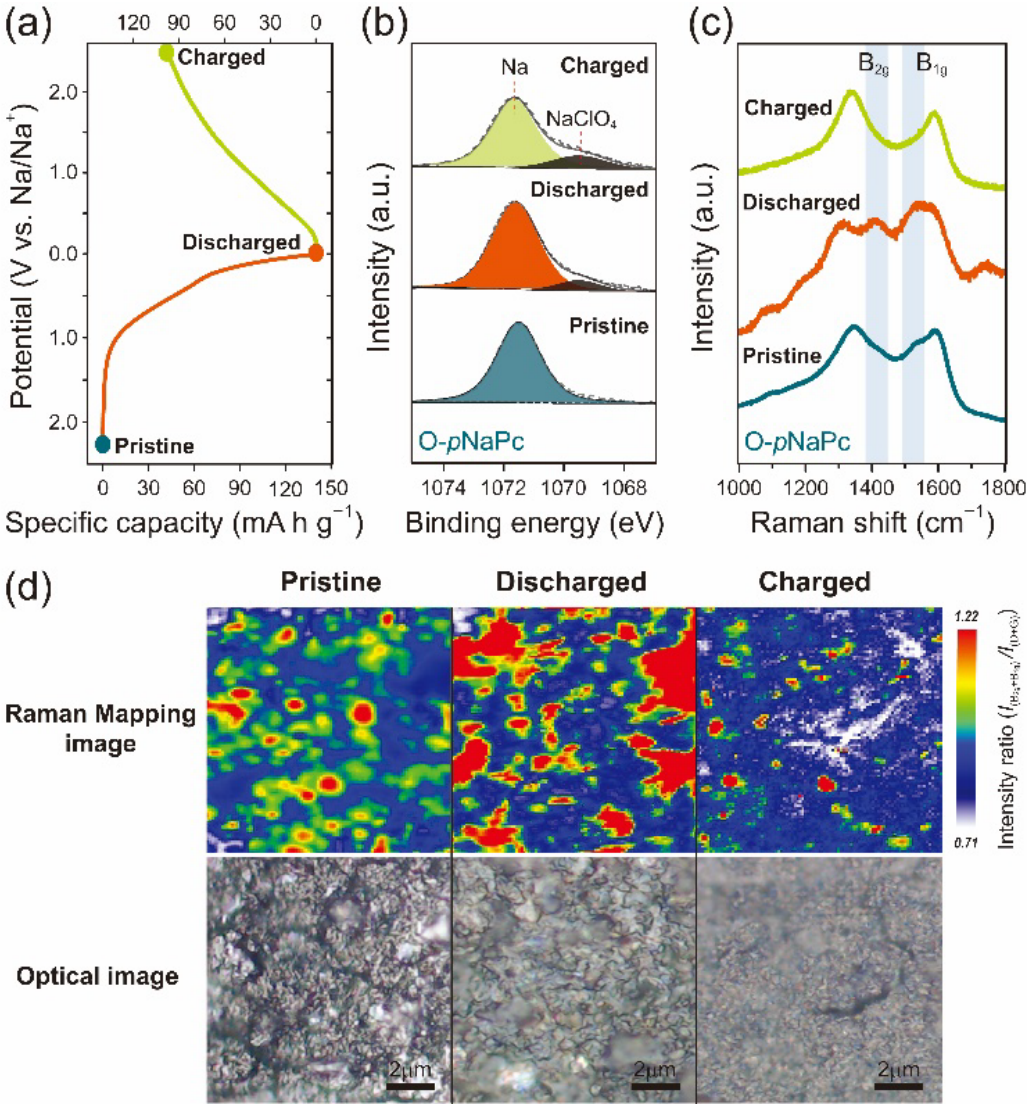

Figure 4. (a) Galvanostatic discharge/charge profile of O-*p*NaPc anodes at a current density of 50 mA g^{-1}. (b) Na 1s XPS spectra and (c) Raman spectra of O-*p*NaPc anode in pristine, charged, and discharged states. (d) *Ex situ* Raman mapping and optical images of O-*p*NaPc anode.

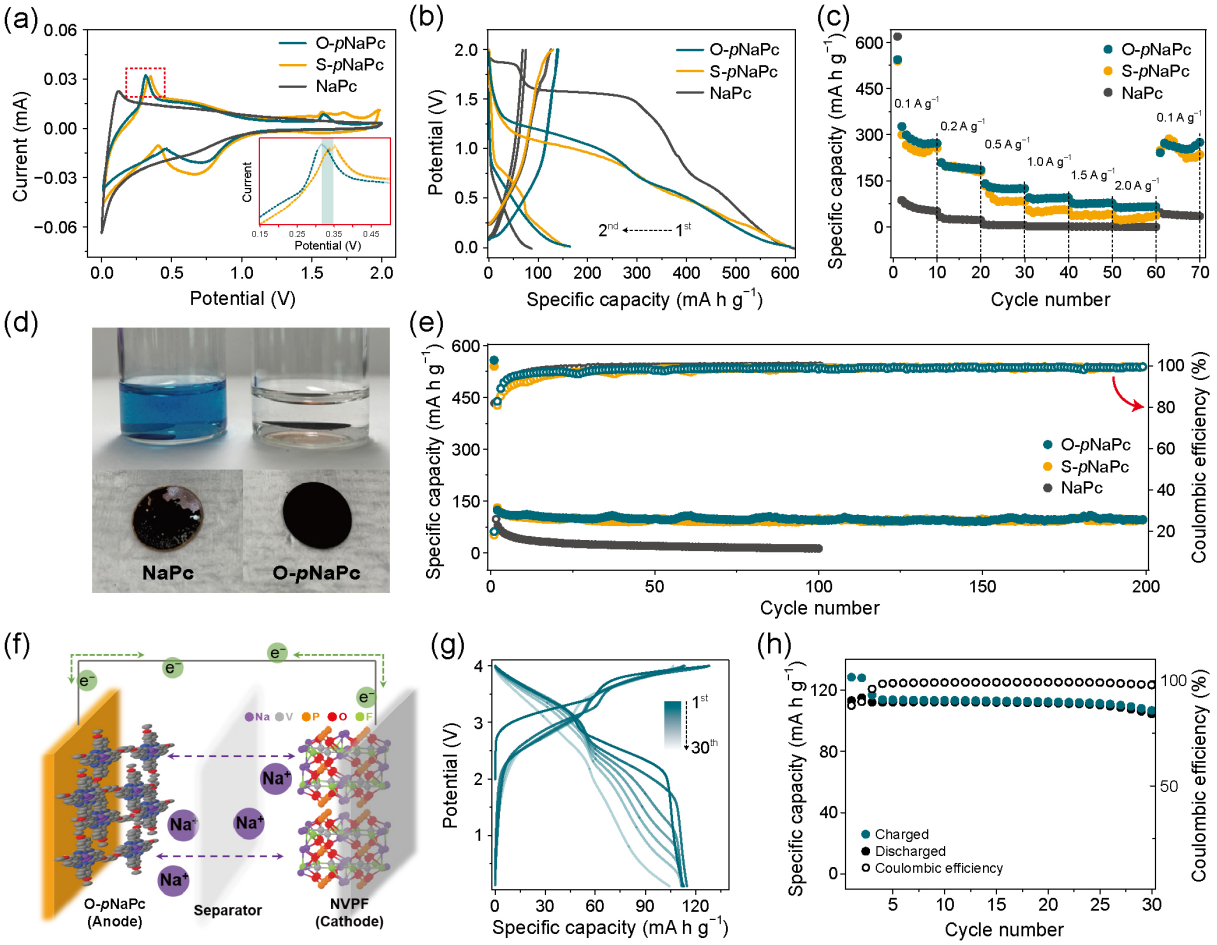

Figure 5. Comparison of (a) CVs at a scan rate of 0.1 mV s^{-1}, (b) galvanostatic discharge/charge profiles at the current density of 0.2 A g^{-1}, and (c) rate performances of NaPc, O-*p*NaPc, and S-*p*NaPc anodes at various current densities. (d) Digital photos demonstrating the solubility of pristine NaPc and O-*p*NaPc anodes in electrolytes (after 10 min, top) and their cycled electrodes (bottom). (e) Cycling performances of NaPc, O-*p*NaPc, and S-*p*NaPc anodes at the current density of 0.2 A g^{-1} for 200 cycles. (f) Schematic illustration of the full-cell configuration. (g) Galvanostatic discharge/charge profiles of the full-cell at the current density of 0.1 A g^{-1}. (h) Cycling performance of the full-cell at the current density of 0.1 A g^{-1} for 30 cycles.